Anisotropic transport and magnetic properties and magnetic-field tuned states of CeZn$_{11}$ single crystals

H. Hodovanets,[1,2] S. L. Bud'ko,[1,2] X. Lin,[2] V. Taufour,[2] M. G. Kim,[1,2,*] D. K. Pratt,[1,2,†] A. Kreyssig,[1,2] and P. C. Canfield[1,2]

[1]*The Ames Laboratory, US DOE, Iowa State University, Ames, Iowa 50011, USA*

[2]*Department of Physics & Astronomy, Iowa State University, Ames, Iowa 50011, USA*

We present detailed temperature- and field-dependent data obtained from magnetization, resistivity, heat capacity, Hall resistivity and thermoelectric power measurements performed on single crystals of CeZn$_{11}$. The compound orders antiferromagnetically at ∼2 K. The zero-field resistivity and thermoelectric power data show features characteristic of a Ce-based intermetallic with crystal-electric-field splitting and possible Kondo lattice effects. We constructed the T-H phase diagram for the magnetic field applied along the easy [110] direction, which shows that the magnetic field required to suppress T_N below 0.4 K is in the range of 45–47.5 kOe. A linear behavior of the $\rho(T)$ data, **H** ∥ [110], was observed only for $H = 45$ kOe for 0.46 K $\leqslant T \leqslant$ 1.96 K followed by the Landau–Fermi-liquid regime for a limited range of fields 47.5 kOe $\leqslant H \leqslant$ 60 kOe. From the analysis of our data, it appears that CeZn$_{11}$ is a local moment compound with little or no electronic correlations arising from the Ce $4f$ shell. The thermoelectric and transport properties of CeZn$_{11}$ are mostly governed by the crystal-electric-field effects. Given the very high quality of our single crystals, quantum oscillations are found for both CeZn$_{11}$ and its nonmagnetic analog LaZn$_{11}$.

I. INTRODUCTION

The broad interest in intermetallic compounds containing Ce is due, in part, to the fact that these compounds sometimes show anomalous electronic and magnetic properties associated with heavy fermions or valence-fluctuation effects.[1–4] A competition between local-moment ordering mediated via the Ruderman-Kittel-Kasuya-Yosida (RKKY) interaction and the onsite Kondo fluctuation of the f electrons leads to the variety of the ground states in these compounds. In addition, the crystal-electric-field (CEF) splitting of the Hunds rule ground-state multiplet J influences the temperature-dependent thermodynamic and transport properties.

With this in mind, polycrystalline samples of CeZn$_{11}$ were investigated by susceptibility and specific-heat measurements for possible heavy-electron behavior.[5] As a result, CeZn$_{11}$ was reported to have a relatively small γ value of 40 mJ/(mol K^2) which was hard to estimate precisely because of the antiferromagnetic (AFM) transition near 2.0 K. It is precisely this relatively low value of the Néel temperature T_N that makes CeZn$_{11}$ a promising candidate for the study of magnetic-field tuning and possible quantum critical point (QCP) effects.

In addition, CeZn$_{11}$ is of interest because two of the first heavy-fermion systems identified were UCd$_{11}$ (Ref. 6) and U$_2$Zn$_{17}$ (Ref. 7). Given the Ce ion's tendency to be more localized, CeZn$_{11}$ may offer the possibility of studying an ordered system that is close to correlated electronic behavior. It should be noted, though, that the study of a similar compound CeCd$_{11}$ of cubic structure (space group $Pm\bar{3}m$), with $T_N = 0.44$ K and $\gamma = 26$ mJ/(mol K^2), revealed that the $4f$ electrons are well localized.[8]

CeZn$_{11}$ crystallizes in tetragonal, $I4_1/amd$, BaCd$_{11}$-type structures. The unit cell contains one unique Ce site with tetragonal point symmetry, and three crystallographically distinct Zn sites. The Ce atom occupies the center of a polyhedron composed with 22 zinc atoms.[9]

In order to gain insight into the anisotropic, low-temperature physical properties of CeZn$_{11}$ and investigate the possibility of a magnetic-field-induced QCP, we grew single crystals and performed transport and thermodynamic measurements down to 0.4 K with applied magnetic fields of up to 140 kOe. We present here anisotropic temperature- and field-dependent magnetic susceptibility, resistivity, Hall effect, heat capacity, and thermoelectric power (TEP) measurements on CeZn$_{11}$. From these measurements, we assembled a T-H phase diagram that shows the evolution of the magnetic-field induced states of CeZn$_{11}$.

II. EXPERIMENT

Single crystals of CeZn$_{11}$, in the form of slightly distorted octahedra (see Fig. 3), were grown from high-temperature binary solutions rich in Zn.[10,11] High-purity, elemental Ce (Ames Laboratory) and Zn (5N, Alfa Aesar) were combined in an alumina crucible in the molar ratio of 1.5:98.5, respectively, and sealed in a silica ampule under 0.25 atm of high-purity argon gas. The ampule, in a 50-ml alumina crucible, placed on an ∼3-cm slab of refractory brick, was heated to 1000 °C, held there for 3 h, cooled over 3 h to 850 °C, and finally cooled down, over 100 h, to 500 °C, at which temperature the excess Zn was decanted using a g-enhancing rotational method.[10,11] Although the single crystals obtained had some of the reflective surfaces covered in Zn flux, the residual flux and/or oxide slag on the crystal surface could be removed by using a dilute acid (0.5 vol% of HCl in H$_2$O) (Ref. 12) or polished off, as in the case of samples for the resistivity, Hall effect, and thermoelectric power measurements.

LaZn$_{11}$ single crystals are useful since they can provide an estimate of the nonmagnetic contribution to the transport and thermodynamic measurements of CeZn$_{11}$. Although CeZn$_{11}$ is the most Zn-rich Ce-Zn binary compound,[13] and as such can be readily grown out of excess Zn, Ref. 14 indicates that

$LaZn_{11}$ is bracketed on either side by the more Zn-rich $LaZn_{13}$ and the less Zn-rich La_2Zn_{17}. This binary phase diagram, if accurate, would imply single-crystal growth of $LaZn_{11}$ out of a binary solution would be difficult. On the other hand, according to Refs. [15] and [16], a substantial liquidus line for $LaZn_{11}$ exists and single crystals should be easily grown. To grow single crystals of $LaZn_{11}$, the high-purity elemental La (Ames Laboratory) and Zn (5N, Alfa Aesar) were put in the molar ratio of 3:97, respectively, into an alumina crucible, then sealed in a silica ampule under 0.25 atm of a high-purity argon gas. The ampule, in a 50-ml alumina crucible, placed on an $\sim$3-cm slab of refractory brick, was heated to $950\,°C$, held there for 2 h, in 1 h cooled to $870\,°C$, held there for 1 h, and then cooled over 75 h to $720\,°C$, at which temperature the excess Zn was decanted. Single crystals of $LaZn_{11}$ obtained were very similar in the morphology to those of $CeZn_{11}$. This result confirms the extended liquidus line shown for $LaZn_{11}$ in Refs. [15] and [16].

Powder x-ray diffraction (XRD) data were collected on a Rigaku MiniFlex diffractometer (Cu $K_{\alpha1,2}$ radiation) at room temperature. Lattice parameters were refined by the LeBail method using RIETICA software.[17] Laue back-reflection patterns were taken with a MWL-110 camera manufactured by Multiwire Laboratories. After the main crystallographic directions were determined, the samples were cut and polished so as to have the applied magnetic field parallel to a particular direction of interest, then the orientation was checked with the help of Laue diffraction, and finally the samples were cut and polished again. The samples for the magnetization measurements were not cut or polished.

Magnetic measurements were carried out in a Quantum Design, Magnetic Property Measurement System (MPMS), SQUID magnetometer. For the magnetization measurements, the sample was glued with Loctite 495 glue to a Kel-F® PCTFE (PolyChloroTriFluoroEthylene) disk, that had been machined so as to tightly fit inside of a transparent plastic straw used as a sample holder for magnetization measurements,[18] with the *c* axis being perpendicular to the disk. To apply the field parallel to the [100] or the [110] direction, the disk with the sample was mounted vertically in-between two straws. Although this measuring protocol allowed for ready orientation of the sample, it also made it hard to have alignments more accurate than $\pm10°$ of desired direction of the applied field. The magnetic signal from disk with the glue (same amount as was used to fix the sample) was subtracted point by point from the total magnetic signal. In order to do that, we acquired the data for the disk with the glue separately using the same temperature and field protocol as for the data collection with the sample. In some instances, the data for the disk were interpolated to match every data point collected for the sample with the disk.

The temperature- and field-dependent resistivity, Hall resistivity, and heat-capacity measurements were performed in the applied fields up to 140 kOe and temperatures down to $\sim$0.4 K in a Quantum Design Physical Property Measurement System (PPMS-14) with a He-3 option. A standard four-probe geometry, ac technique ($f = 16$ Hz, $I = 3$–0.3 mA), was used to measure the electrical resistance of the samples. Electrical contact to the samples was made with platinum wires attached to the samples using EpoTek H20E silver epoxy. To calculate the resistivity of two samples of $CeZn_{11}$ and a sample of

$LaZn_{11}$, the cross-sectional area and the distance between the midpoints of the two voltage contacts were used. For the two directions of current flow for $CeZn_{11}$, $l = 0.69 \pm 0.01$ mm for **I** $\|$ [001] and $l = 0.94 \pm 0.01$ mm for **I** $\|$ [010], the width of both voltage contacts together was 0.27 ± 0.01 mm for **I** $\|$ [001] and 0.26 ± 0.01 mm for **I** $\|$ [010]. The virtually equal resistivity values for both current orientations is most likely a coincidence due to the chosen criterion of estimation of the distance between the two voltage contacts. If the distance between the outside and inside ends of contacts is used, then the value of resistivity will be 28% smaller and 64% larger (**I** $\|$ [001]), respectively, and 22% smaller and 38% larger (**I** $\|$ [010]), respectively, of that calculated for the criterion chosen above. We believe that in the present case, the larger error in the calculation of the resistivity comes from estimating the distance between the voltage contacts rather than from the measurements of the cross-section area of the samples. The cross-section areas (W$\times$H) of the samples used in this work were 0.28×0.12 mm^2 (**I** $\|$ [001]) and 0.17×0.08 mm^2 (**I** $\|$ [010]).

The same criterion was used to determine the resistivity of $LaZn_{11}$ single crystals. The distance between the midpoints of the voltage contacts was 2.70 ± 0.05 mm and the width of both voltage contacts together was 0.39 ± 0.05 mm. If the distance between the outside and inside ends of contacts is used, then the value of resistivity will be 4% smaller and 11% larger, respectively, of that calculated with the criterion described above. The cross-section area of the sample was 0.17×0.09 mm^2 (W$\times$H).

The heat capacity of the samples was measured with the help of a relaxation technique. The measured background heat capacity, which includes the sample platform and grease for all necessary (H,T) values, was accounted for in the final results. The heat capacity of $LaZn_{11}$ was measured in the same temperature range and was used to estimate the nonmagnetic contribution to the heat capacity of $CeZn_{11}$.

A four-wire geometry, ac technique, was used to collect the Hall resistivity data. The polarity of the magnetic field was switched to remove any magnetoresistive components due to the misalignment of the voltage contacts. The current contacts were placed on two opposite side faces of the plate-shape crystals. The voltage contacts were placed on the other two remaining side faces of the crystals. All four contacts were made with Pt wires and EpoTek H20E silver epoxy.

The thermoelectric power (TEP) measurements were performed by a dc, alternating heating (two heaters and two thermometers) technique[19] using a Quantum Design PPMS to provide the temperature environment between 2 and 300 K. The samples were mounted directly on the gold-plated surface of the SD package of the Cernox thermometers using Du-Pont 4929N silver paste to ensure thermal and electrical contact.

III. RESULTS AND ANALYSIS

A. Basic physical properties

The powder x-ray diffraction patterns collected on the ground single crystals of $CeZn_{11}$ and $LaZn_{11}$ are shown in Figs. 1 and 2, respectively. X-ray diffraction measurements confirmed the crystal structure of $CeZn_{11}$ and $LaZn_{11}$. Small
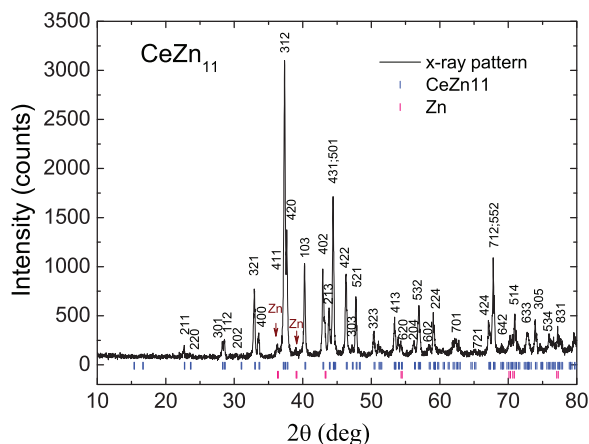
FIG. 1. (Color online) Powder x-ray diffraction pattern of finely ground $CeZn_{11}$ single crystals. The peaks that belong to $CeZn_{11}$ are indexed to a tetragonal unit cell with $a = 10.67 \pm 0.02$ Å and $c = 6.87 \pm 0.01$ Å. The relatively few, low-intensity peaks that can be associated to Zn are not indexed, however, the markers of the peaks positions are given.

traces of Zn, from residual flux, can be seen in both patterns. The lattice parameters of $CeZn_{11}$ obtained from the LeBail fit are $a = b = 10.67 \pm 0.02$ Å and $c = 6.87 \pm 0.01$ Å and are consistent with the reported unit cell.[9] The lattice parameters of $LaZn_{11}$ obtained from the LeBail fit of the x-ray pattern are $a = b = 10.69 \pm 0.02$ Å and $c = 6.89 \pm 0.01$ Å and are also consistent with those published in the literature.[20]

Due to the as-grown, single crystals' ambiguous morphology, slightly distorted octahedra [see Fig. 3(d)], it is hard to visually identify the orientation of the facets. In order to determine the main crystallographic directions, Laue back-reflection patterns were taken. Figure 3(a) shows an x-ray Laue backscattering pattern of the [001] direction with a fourfold rotation symmetry and four mirror planes with 45° angles between each other. Figure 3(b) shows an x-ray Laue
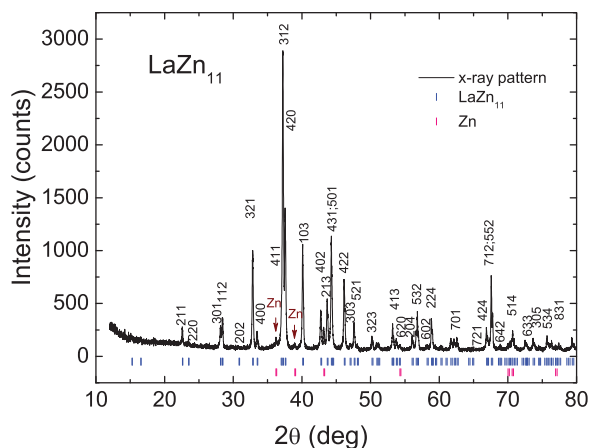

FIG. 2. (Color online) Powder x-ray diffraction pattern of finely ground $LaZn_{11}$ single crystals. The peaks that belong to $LaZn_{11}$ are indexed to a tetragonal unit cell with $a = 10.69 \pm 0.02$ Å and $c = 6.89 \pm 0.01$ Å. The relatively few, low-intensity peaks that can be associated to Zn are not indexed, however, the markers of the peaks positions are given.
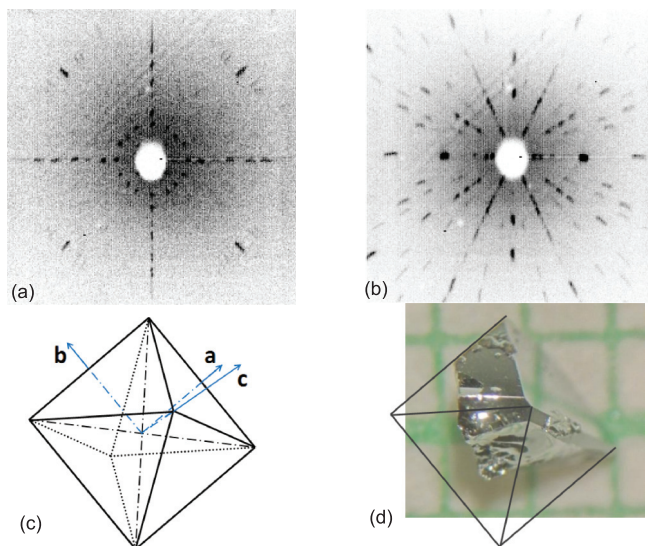

FIG. 3. (Color online) (a) X-ray Laue backscattering pattern showing a fourfold rotation symmetry of the [001] direction, (b) x-ray Laue backscattering pattern showing a twofold rotation symmetry of the [110] direction, (c) a sketch of the sample with the main crystallographic directions, and (d) the picture of the sample with the mirrored triangular surface being the (101) plane. Solid lines show the extension of the sample to match the sketch in (c).

backscattering pattern of the [110] direction with a twofold rotation symmetry and two mirror planes perpendicular to each other. Figure 3(c) shows a sketch of an idealized, pseudo-octahedral crystal with the main crystallographic directions identified. Figure 3(d) shows the picture of an actual sample (truncated by growth and separation) with the mirrored triangular surface being the (101) plane. Solid lines show the extension of the sample to match the sketch in Fig. 3(c). [Note: The c axis goes through the tip (apex) of the crystal that points nearly out of the page whereas the a and b axes bisect the edges of the pseudo-octahedron at roughly 45° and 135°.] After the main crystallographic directions were determined using the Laue back-reflection technique, the samples were cut and polished so as to have the applied magnetic field parallel to a particular direction of interest. The samples for the magnetization measurements were not cut or polished.

The anisotropic temperature-dependent magnetization divided by the applied field data $M(T)/H$ of $CeZn_{11}$ are shown in Fig. 4(a), where the magnetic field was applied along the [100], [110], [001], and [101] directions. An arrow marks the value of $T_N = 2.00 \pm 0.03$ K that was obtained from the maximum in $d(\chi T)/dT$[21] [$\chi = M(T)/H$ at small fields for which $M(H)$ at constant temperature is linear]. The magnetic susceptibilities for the field applied along the [100] and [110] directions are essentially the same and are about 10 times larger at low temperature than the magnetic susceptibility for the field applied along the [001] direction. As would be expected, when the field is applied along the [101] direction, $M(T)/H$ falls between the data for **H** ∥ [100] and **H** ∥ [001]. The inset to Fig. 4(a) displays the temperature-dependent inverse magnetic susceptibilities $H/M(T)$ for the field applied along the [100], [001], and of polycrystalline average taken as $\chi_{poly} = (2\chi_{100} + \chi_{001})/3$. The modified Curie-Weiss law fit of
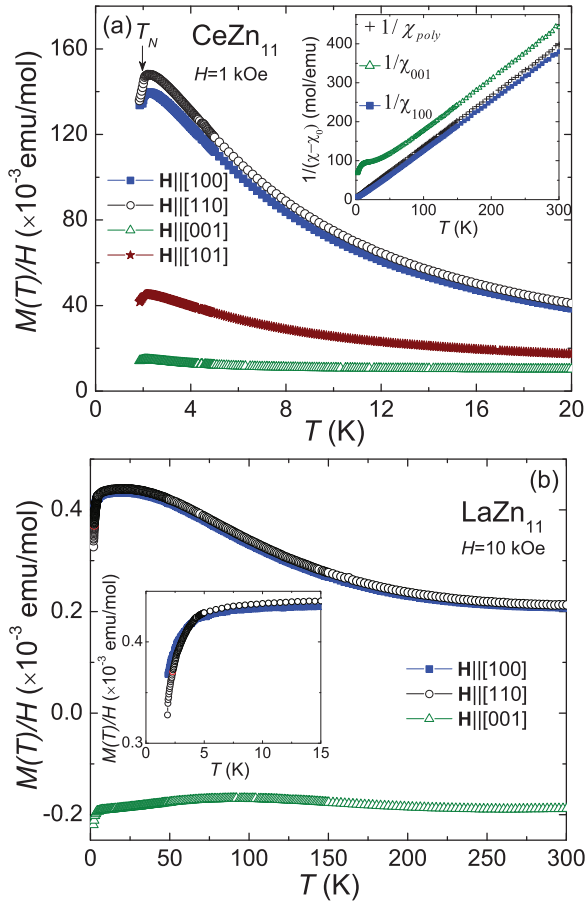
FIG. 4. (Color online) (a) Temperature-dependent magnetic susceptibility $M(T)/H$ of CeZn$_{11}$, with the magnetic field applied along the [100], [110], [001], and [101] directions. The inset displays temperature-dependent, inverse magnetic susceptibilities for the field applied along the [100], [001], and of polycrystalline average $\chi_{\text{poly}} = (2\chi_{100} + \chi_{001})/3$. (b) Temperature-dependent magnetic susceptibility $M(T)/H$ of LaZn$_{11}$, with the magnetic field applied along the [100], [110], and [001] directions. The inset shows the enlarged low-temperature part of the $M(T)/H$. We would like to draw the reader's attention to the difference in the vertical scales of (a) and (b).

the magnetic susceptibility in the form $\chi = \chi_0 + C/(T - \theta)$ of the polycrystalline average above 50 K results in $\theta_p \simeq -5.6 \pm 1.0$ K and $\mu_{\text{eff}} \simeq 2.48 \pm 0.01\ \mu_B/\text{Ce}^{3+}$ which is close to the Ce^{3+} free-ion value of 2.54 μ_B. The results of the modified Curie-Weiss law fit are listed in Table I.

The $M(T)/H$ data for LaZn$_{11}$ are shown in Fig. 4(b), where the magnetic field was applied along the [100], [110], and [001] directions. $M(T)/H$ for **H** ∥ [100] and [110] are positive whereas $M(T)/H$ for **H** ∥ [001] is negative,

TABLE I. Results of the modified Curie-Weiss law fit of the magnetic susceptibility.

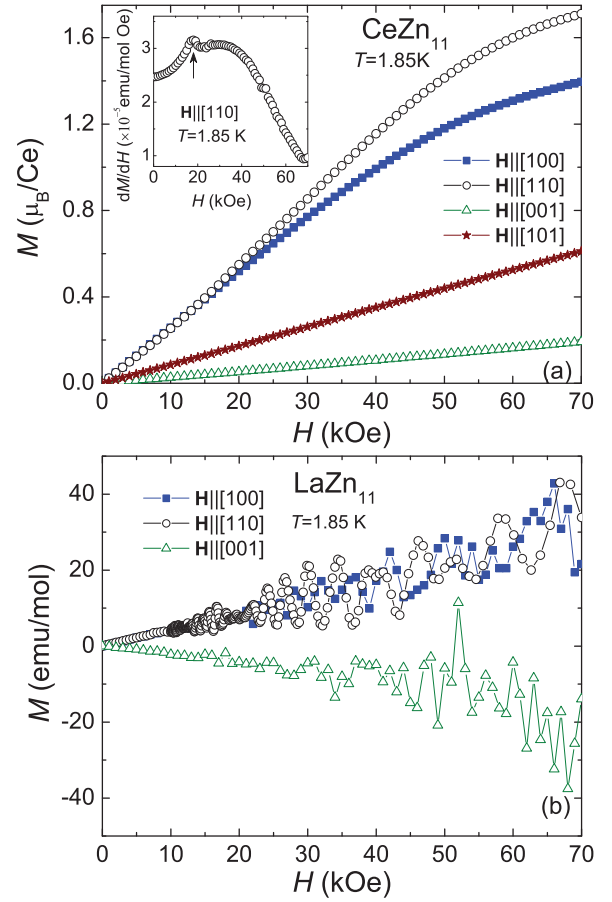| χ	χ_0 (emu/mol)	θ (K)	$\mu_{\text{eff}}(\mu_B)$
χ_{100}	$(-7.8 \pm 0.1) \times 10^{-4}$	1.2 ± 0.5	
χ_{110}	$(-7.8 \pm 0.1) \times 10^{-4}$	-1.6 ± 0.1	
χ_{001}	$(-1.9 \pm 0.1) \times 10^{-4}$	-31 ± 1	
χ_{poly}	$(-5.6 \pm 0.1) \times 10^{-4}$	-5.6 ± 1.0	2.48 ± 0.01

FIG. 5. (Color online) (a) Magnetization isotherms $M(H)$ of CeZn$_{11}$ at 1.85 K for the magnetic field applied along the [100], [110], [001], and [101] directions. The inset: dM/dH versus H for **H** ∥ [110] with the arrow denoting a broad metamagneticlike feature seen in $M(H)$. (b) Magnetization isotherms $M(H)$ of LaZn$_{11}$ at 1.85 K for the magnetic field applied along the [100], [110], and [001] directions.

reflecting anisotropy of the Pauli and Landau terms relative to the Larmor diamagnetic susceptibility. The apparent drop in $M(T)/H$ of LaZn$_{11}$ below ~10 K is due to filling of Landau levels associated with quantum oscillations shown in detail in Fig. 5(b).

When the χ_0 values found for CeZn$_{11}$ are compared with the high-temperature $\chi(T)$ data of LaZn$_{11}$, there is a good agreement for **H** ∥ [001] and poor agreement between the in-plane χ_0 values which is most likely due to delicate balance of terms with different signs (Pauli paramagnetism versus Landau and Larmor diamagnetism).

Magnetic isotherms $M(H)$ of CeZn$_{11}$, shown in Fig. 5(a), were taken at 1.85 K for the magnetic field applied along the same orientations as the $M(T)/H$ in Fig. 4(a). The magnetization does not saturate in any direction for our highest field of 70 kOe. The magnetic moment is highly anisotropic and reaches the highest value of 1.7 μ_B/Ce^{3+} at 70 kOe for the magnetic field applied along the [110] direction, which is below the theoretical saturated value of 2.1 μ_B for the free Ce^{3+} ion. In addition, $M(H)$ for the magnetic field along the [110] direction shows a broad metamagneticlike feature centered at about 18 kOe visible as a non-Brillouin-type upward curvature in the data, but more clearly seen in dM/dH
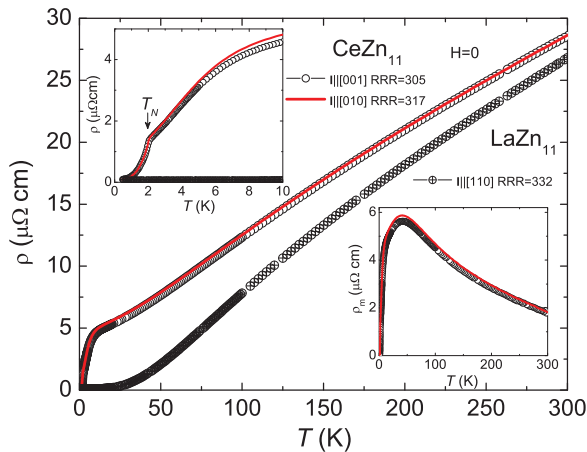
FIG. 6. (Color online) Zero-field, temperature-dependent resistivity $\rho(T)$ data of CeZn$_{11}$ and LaZn$_{11}$. The inset in the upper left shows an enlarged, low-temperature part of the resistivity with the AFM transition T_N marked with an arrow. The inset in the lower right shows the magnetic part of the resistivity $\rho_m = \rho(\text{CeZn}_{11}) - \rho(\text{LaZn}_{11})$. The data shown in the insets are the same as shown in the main panel of the figure.

plot shown in the inset to Fig. 5(a). As will be shown in further detail below, this feature is associated with the suppression of T_N to below 1.85 K at this field.

Magnetic isotherms $M(H)$ of LaZn$_{11}$, shown in Fig. 5(b), were taken at 1.85 K for the magnetic field applied along the same orientations as the $M(T)/H$ in Fig. 4(b). Consistent with the $M(T)$ data, $M(H)$ for **H** ∥ [001] is negative whereas $M(H)$ for **H** ∥ [100] and **H** ∥ [110] are positive. The de Haas–van Alphen (dHvA) oscillations are clearly seen setting in near ∼10 kOe in the $M(H)$ for all field orientations. Analysis of the quantum oscillations is given in the Appendix. Change in the amplitude of the quantum oscillations with temperature is the origin of the drop in the $M(T)/H$ seen in Fig. 4(b). As shown in the inset to Fig. 4(b), for $H = 10$ kOe, the Landau levels start to fill below $T \sim 10$ K.

The zero-field, temperature-dependent resistivity $\rho(T)$ data of CeZn$_{11}$ for current flow along the [010] and [001] directions are presented in Fig. 6. The $\rho(T)$ plots show a broad shoulder, characteristic of that of Kondo compounds, at around 10 K followed by a sharp change of the slope and a kink (see upper-left inset to Fig. 6) corresponding to the AFM transition at 1.96 ± 0.05 K estimated from the maximum in $d\rho/dT$.[22] The broad shoulder may also have some contribution associated with the relatively small value of the CEF splitting, which stems from the very symmetric, local environment of the Ce ion (in a shell of 22 Zn atoms).[9] The $\rho(T)$ data for both current directions are similar, although, as was mentioned above, the virtually equal resistivity values for both current orientations is most likely a coincidence and merely means that $\rho(T)$ has relatively low anisotropy. The residual resistivity ratios (RRR) of the two samples are 305 for **I** ∥ [001] and 317 for **I** ∥ [100].

The zero-field, temperature-dependent resistivity $\rho(T)$ data of LaZn$_{11}$ are also shown in Fig. 6 for comparison. LaZn$_{11}$ is the nonmagnetic, isostructural variant of CeZn$_{11}$, and $\rho(T)$ of LaZn$_{11}$ gives an estimate of the nonmagnetic contribution to the resistivity of CeZn$_{11}$. With the assumption that the

resistivity of LaZn$_{11}$ is isotropic, we calculated the magnetic resistivity $\rho_m = \rho(\text{CeZn}_{11}) - \rho(\text{LaZn}_{11})$, for each of the shown data sets (lower-right inset to Fig. 6). ρ_m shows a broad peak near 40 K which may be associated with a combination of possible Kondo physics and the certain thermal depopulation of the exited CEF level as the temperature is decreased.

Heat-capacity data $C_p(T)$ for CeZn$_{11}$ [Fig. 7(a)] show a clear, sharp λ anomaly at 2.00 ± 0.06 K, which is consistent with the ordering temperature values inferred from magnetization and resistivity measurements [Fig. 7(b)], all of which are consistent with a second-order transition from the paramagnetic to an AFM ordered state. A broad peak at around 5 K corresponds to a Schottky anomaly arising from the CEF splitting of the Hund's rule ground-state multiplet. The sum of the electronic and lattice contribution to the specific heat of CeZn$_{11}$ may be approximated by the specific heat of LaZn$_{11}$, which is also shown in Fig. 7(a). The electronic specific-heat coefficient (γ) and the Debye temperature (Θ_D) estimated from the relation $C_p/T = \gamma + \beta T^2$ for LaZn$_{11}$ are 10.2 mJ/(mol K^2) [or 0.85 mJ/(mol K^2 atom)] and 353 K [$\beta = 0.53$ mJ/(mol K^4)], respectively, and are similar to the ones reported in Ref. 5. Because of the AFM order at 2 K and the higher-temperature broad peak associated with CEF effect, γ and Θ_D for CeZn$_{11}$ can not be estimated from the relation $C_p/T = \gamma + \beta T^2$. As a matter of fact, the fit of the C_p/T versus T^2, for $T > T_N$, gave γ values in the range 100–200 mJ/(mol K^2) depending on the temperature range chosen. C_p/T of CeZn$_{11}$ has a value of 100 mJ/(mol K^2) at 0.4 K and is still significantly larger than the value of LaZn$_{11}$ [11.9 mJ/(mol K^2)] at the same temperature.

The magnetic contribution to the specific heat of CeZn$_{11}$, calculated as $C_m = C_p(\text{CeZn}_{11}) - C_p(\text{LaZn}_{11})$, allows for the inference of the change in the entropy by integrating C_m/T with respect to T, shown in Fig. 7(c). The very slight mass correction to the LaZn$_{11}$ data[23] was not done since the mass-correction factor $\Theta_D(\text{CeZn}_{11})/\Theta_D(\text{LaZn}_{11})$ is 0.9990. The entropy recovered up to T_N is $0.64R \ln 2$ and is consistent with the ordered state emerging from a CEF ground-state doublet with the first excited-state doublet located nearby. According to Ref. 24, for a two-level system that has equal degeneracy, the maximum of the Schottky anomaly occurs at $T_m = 0.42\delta$ and $C_{\text{Sch}}(\text{max}) = 3.64$ J/(mol K). δ is the energy separation between two levels. For CeZn$_{11}$, $C_{\text{Sch}}(\text{max}) = 3.62$ J/(mol K) at $T_m \sim 5.31$ K, leading to $\delta \sim 12.6$ K. An alternate way to estimate the CEF splitting is to fit the C_m data to the Schottky anomalies assuming that the $J = \frac{5}{2}$ multiplet is split into three doublets by tetragonal point symmetry. Taking into account that the peak associated with the AFM transition is very close to the Schottky anomaly, instead of fitting the C_m data, we modeled the Schottky anomalies assuming that the energies of the first and second doubly degenerate excited states are Δ_1 and Δ_2 and added the modeled Schottky anomalies to the heat-capacity data of LaZn$_{11}$. The result is illustrated by a dashed curve in Fig. 7(a). By adjusting the values of Δ_1 and Δ_2, we obtained the best agreement with the experimental data, for $T > T_N$, for $\Delta_1 = 12.2$ K and $\Delta_2 = 65$ K, which are slightly higher than the ones reported in Ref. 5. If we perform the fit of $C_{\text{mag}}(T)$ as $\gamma'T + C_{\text{Sch}}$ (with the temperature region of the AFM ordering excluded), where C_{Sch} is the contribution of the modeled Schottky anomalies, then $\gamma' = 24.3$ mJ/(mol
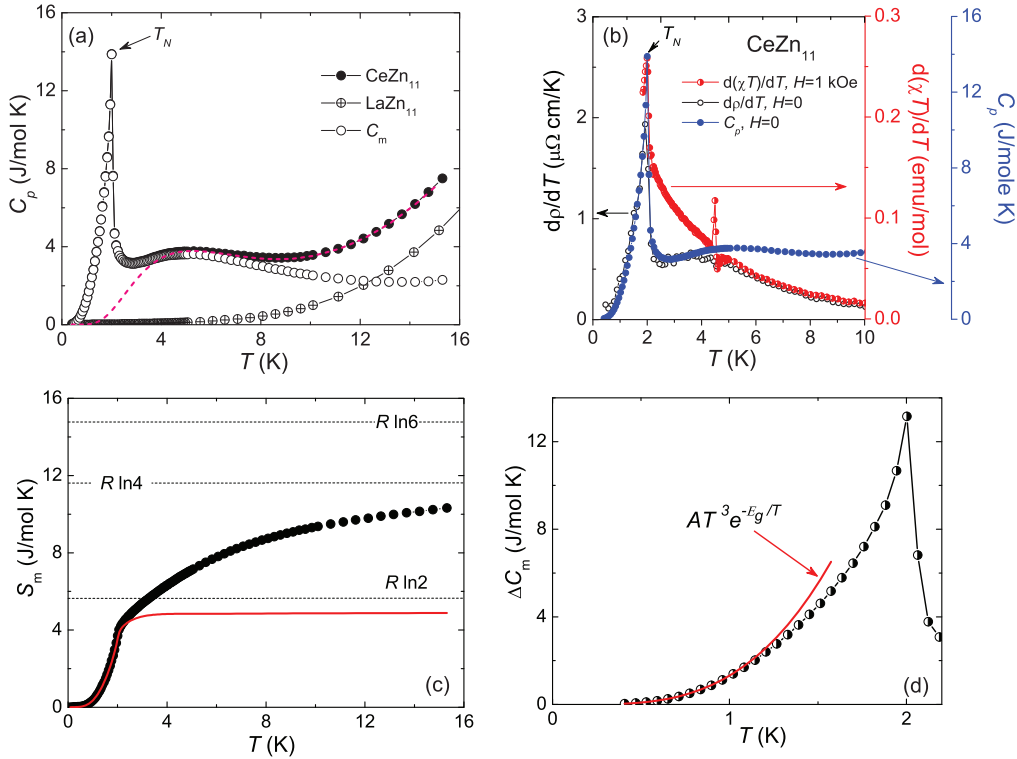
FIG. 7. (Color online) (a) Heat capacity $C_p(T)$ of CeZn$_{11}$ ($\bullet$: total), $\oplus$: heat capacity of LaZn$_{11}$ (electronic and lattice), and $\circ$: magnetic [$C_m = C_p$(CeZn$_{11}$) $- C_p$(LaZn$_{11}$)]. Dashed curve: modeled Schottky anomaly assuming that the energies of the first and second excited states are $\Delta_1 = 12.2$ K and $\Delta_2 = 65$ K added to heat-capacity data of LaZn$_{11}$. (b) dρ/dT, d(χT)/dT, and C_p as a function of temperature. The $\rho(T)$ data set was smoothed with the adjacent-averaging method with two points of window before derivative was taken. (c) Magnetic entropy S_m calculated by integrating C_m/T ($\bullet$) and $\Delta C_m/T$ (line). (d) $\Delta C_m = C_p$(CeZn$_{11}$) $- C_p$(LaZn$_{11}$) $- C_{\text{Sch}}$, where C_{Sch} is the contribution of the modeled Schottky anomalies, as a function of temperature. Red line is the low-temperature fit of the data with the function $AT^3 e^{-E_g/T}$, which is expected for the magnon specific heat of an antiferromagnet with the energy gap E_g in the magnon dispersion relation (Refs. 24 and 25).

K^2) and $\Delta_1 = 11.3$ K and $\Delta_2 = 71.4$ K. In this case γ(total) $= \gamma$(LaZn$_{11}$) $+ \gamma' = 34.6$ mJ/(mol K^2) for CeZn$_{11}$. It should be noted that $\gamma = 34.6$ mJ/(mol K^2) is a small value for a strongly correlated Ce-based system.

To better understand the functional dependence of the magnetic specific heat at low temperatures, below the AFM transition, we fitted the data below 1 K of $\Delta C_m = C_p$(CeZn$_{11}$) $-$ C_p(LaZn$_{11}$) $- C_{\text{Sch}}$, where C_{Sch} is the contribution of the modeled Schottky anomalies, with the function $AT^3 e^{-E_g/T}$, which is expected for the magnon specific heat of antiferromagnet with the energy gap E_g in the magnon dispersion relation.[24,25] The result of the fit is illustrated as a solid line in Fig. 7(d). From the fit, we obtained $E_g = 0.66$ K. An integral of $\Delta C_m/T$, the magnetic entropy, is shown as a solid line in Fig. 7(c). The magnetic entropy is $\sim 0.85 R \ln 2$ which is consistent with the ordered state emerging from the CEF state doublet. As stated in this paragraph above, ΔC_m has only γ(LaZn$_{11}$) excluded and addition of a linear term γT to the magnon contribution fit results in $\gamma = 0$. The small value of γ(CeZn$_{11}$) $\approx \gamma$(LaZn$_{11}$) suggests the absence of strong correlations.

The zero-field, temperature-dependent thermoelectric power (TEP) $S(T)$ data of CeZn$_{11}$ are plotted in Fig. 8. Since the base temperature for the TEP measurements is 2.1 K, the AFM transition for CeZn$_{11}$ was not observed in the TEP measurements. The value of the TEP is positive above 4 K, signifying that hole-type carriers dominate the thermoelectric

transport in this material. The temperature dependence of the TEP for CeZn$_{11}$ is reminiscent of $S(T)$ of the noble metals or Zn,[26] although it does have a complex behavior at low temperature rather similar to that of the Ce-based heavy-fermion compounds which usually display one or more peaks.[27–29] The absolute value of the TEP is not anomalously
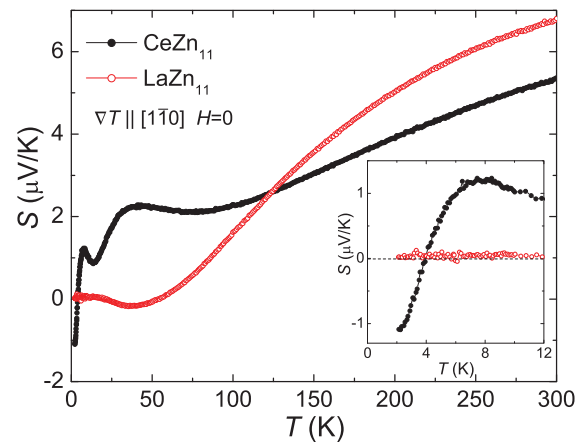

FIG. 8. (Color online) Zero-field, temperature-dependent thermoelectric power $S(T)$ of CeZn$_{11}$ and LaZn$_{11}$. The inset: expanded, low-temperature portion of the plot.

large (TEP of LaZn$_{11}$ being larger for $T > 130$ K) and the temperature dependence of the TEP is almost linear above 125 K. Two positive maxima, at ∼8 and ∼40 K, and a positive minimum at ∼13.6 K are observed in the $S(T)$ at temperatures below 60 K. Since S must vanish as T tends to zero, our data (inset to Fig. 8) suggest the occurrence of at least one more negative extremum in the TEP data as the temperature is lowered below 2.1 K. The position of the peak at ∼40 K is very similar to the one found in the TEP of Zn (with the temperature gradient perpendicular to the hexagonal axis[30]) that has been attributed to the phonon drag contribution to the TEP.

The zero-field $S(T)$ data of LaZn$_{11}$ are also plotted in Fig. 8. As can be seen from the inset to Fig. 8, $S(T)$ of LaZn$_{11}$ tends to zero as temperature is lowered. The broad negative minimum at ∼37 K is probably due to the phonon drag contribution to the TEP.[26,31]

Based on our modeled Schottky anomalies, the lower temperature of CEF splitting Δ_1 is likely to be the origin of the broad shoulder observed in $\rho(T)$ at around 10 K and also of positive maximum in the TEP at around 8 K. On the other hand, the origin of the positive maximum in the TEP around 40 K, the position of which is weakly affected by the applied magnetic field (shown in Fig. 15) and which is at similar temperature as the broad peak in $\rho_m(T)$, may be ascribed to an interplay of Kondo, crystal-field, and phonon drag effects. If we assume that the θ_D of CeZn$_{11}$ is very close to that of LaZn$_{11}$, then the peak due to the phonon-drag contribution to the TEP data should be expected at ∼0.1–0.2θ_D (Refs. 26 and 31) which translates into a 35–70 K temperature range. The negative minimum at ∼37 K in $S(T)$ of LaZn$_{11}$ and positive maximum at ∼40 K in $S(T)$ of CeZn$_{11}$ are both in this temperature range.

B. Measurements in applied magnetic field ($\mathbf{H} \parallel$ [110])

Given its relatively low-T_N value, coupled with our ability to grow very high-quality, large RRR single crystals, we decided to determine the T-H phase diagram for CeZn$_{11}$ and look for possible quantum critical effects. Since Fig. 5(a) shows that the magnetization for the magnetic field applied along the [110] direction is larger than that for the field applied along any other measured direction, indicating that [110] is likely to be an easy axis, we will focus our attention on the field dependence of measurements with $\mathbf{H} \parallel$ [110]. Figure 9 shows low-temperature $\rho(T)$ curves for CeZn$_{11}$ taken at different applied fields for $\mathbf{H} \parallel$ [110] with each subsequent data set shifted upward by 0.3 $\mu\Omega$ cm for clarity. The AFM transition temperature T_N was taken as the maximum in dρ/dT (Ref. 22) and is marked with arrows for $H \leqslant 42.5$ kOe. As the magnetic field is increased, the kink associated with the AFM transition temperature moves to the lower temperatures and is suppressed below our base temperature of 0.46 K by $H = 45$ kOe. For the applied field of 45 kOe, the low-temperature $\rho(T)$ functional dependence appears to be essentially linear $\rho(T) \sim T$ from base temperature of 0.46 K to ∼2 K. Finally, for the applied field larger than 60 kOe, at low temperature an upturn in the $\rho(T)$ appears.

$\rho(H)$ isotherms for CeZn$_{11}$ are shown in Fig. 10(a). The fields of transition, from the low-field ordered state to a higher-field, most likely saturated paramagnetic, state are
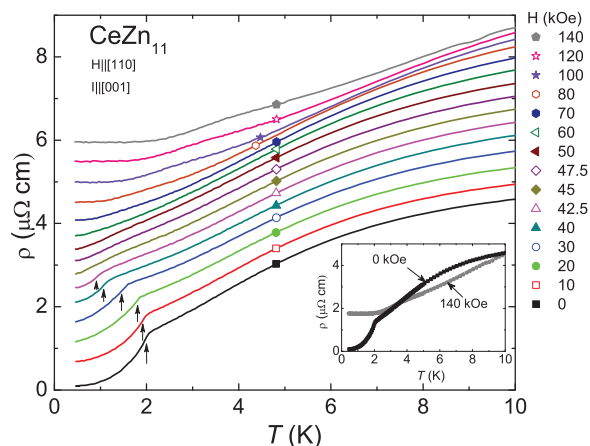

FIG. 9. (Color online) Low-temperature parts of $\rho(T)$ curves for CeZn$_{11}$ taken at different applied fields for $\mathbf{H} \parallel$ [110]. Subsequent data sets are shifted upward from each other by 0.3 $\mu\Omega$ cm for clarity. For $H \leqslant 42.5$ kOe, the arrows denote the transition temperature T_N inferred from dρ/dT. The inset shows the resistivity curves for $H = 0$ and 140 kOe without any offset.

denoted by arrows. This field of magnetic ordering was determined by the intersection of two lines that go through the dρ/dH data presented in Fig. 10(b). Another feature in the field-dependent resistivity, marked with solid dots in Fig. 10(a), appears above 45 kOe and can be seen more clearly as a minimum in the dρ/dH data in Fig. 10(b). This feature moves to the higher fields as the temperature is increased. Small-amplitude Shubnikov–de Haas (SdH) oscillations can be seen for the applied magnetic fields larger than 70 kOe in the lower-temperature data in $\rho(H)$ and even more so in d$\rho(H)$/dH.

In order to better understand the magnetoresistance of CeZn$_{11}$ away from the features associated with metamagnetic transitions (i.e., in the ordered and in the paramagnetic states), we plotted the data for the highest and lowest field and temperature on the Kohler plot shown in Fig. 11. The graph with the data taken for all applied fields and temperatures measured is shown in the Appendix. The Kohler's rule is stated as $\Delta\rho/\rho_0 = F(H/\rho_0)$ where ρ is the resistivity component $\rho_{xx}(H_z)$, ρ_0 is the zero-field resistivity at a given temperature, and $F(H/\rho_0)$ is a universal function for the particular material regardless of temperature or impurity content. This rule is applicable to single-band metals, for which the number of carriers does not vary with temperature or impurity content to a very good approximation. Consequently, variation in ρ_0 reflects one single relaxation time (one scattering mechanism). The magnetoresistance of many metals and semimetals is known to follow the Kohler's rule[32,33] and several rare-earth-bearing intermetallic compounds (and series) have shown remarkably large and structured magnetoresistivities that can be understood in the context of Kohler's law. It is clear from the Kohler plot that the magnetoresistance of CeZn$_{11}$ fails to show a single power-law dependence for all fields and temperatures, but instead appears to have two manifolds: one in the ordered state $[H/\rho(0,T)]^{0.7}$ and one in the paramagnetic state $[H/\rho(0,T)]^1$ represented by the dashed and solid lines, respectively, in Fig. 11.
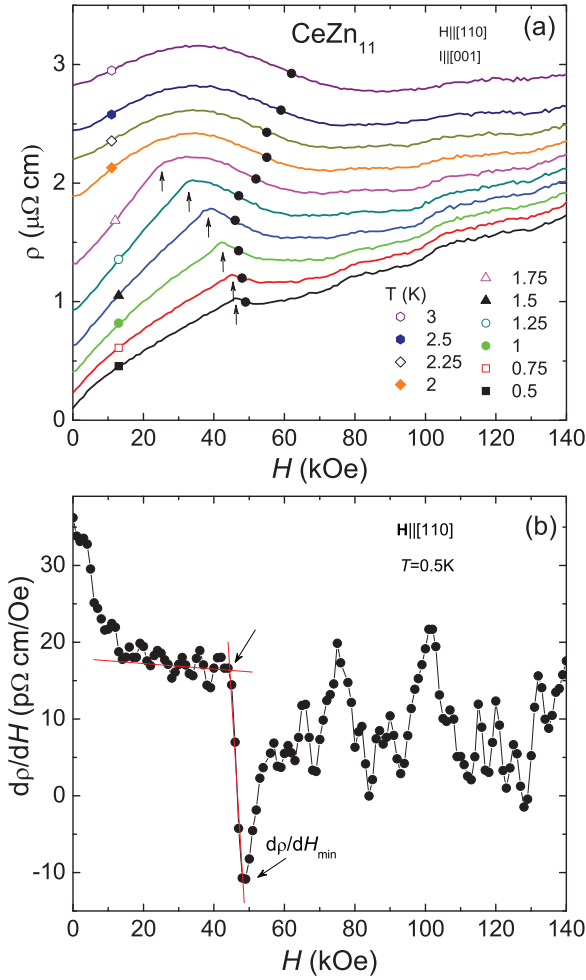
FIG. 10. (Color online) (a) $\rho(H)$ ($\mathbf{H} \parallel$ [110]) isotherms for CeZn$_{11}$. Subsequent data sets are shifted upward by 0.1 $\mu\Omega$ cm from each other. The arrows denote the fields of magnetic ordering that were determined by the intersection of two lines that go through the $d\rho/dH$ data shown in (b). Solid dots represent the position of the minimum in the $d\rho/dH$ data in (b). (b) $d\rho/dH$ at 0.5 K as a function of magnetic field, with the criterion for the field of magnetic ordering and the minimum $(d\rho/dH)_{min}$. The $\rho(H)$ data set was smoothed with the adjacent-averaging method with a 2 points of window before derivative was taken.

The heat-capacity measurements of CeZn$_{11}$, taken with different applied magnetic fields $\mathbf{H} \parallel$ [110], are plotted in Fig. 12. The arrows in Figs. 12(a), 12(b), and 12(c), indicating the position of the peaks associated with the magnetic ordering, are consistent with the resistivity measurements described above. As the applied magnetic field is increased, the sharp peak corresponding to the AFM transition moves to lower temperatures and decreases in size. From $H = 47.5$ to 52.5 kOe, the lower-field peak in the specific heat evolves into a rather broad shoulder [see Fig. 12(c)].

Figure 13 presents the heat-capacity data of CeZn$_{11}$ as a function of magnetic field at constant temperatures of 0.5, 1, and 3 K. At 0.5 K, field-dependent specific heat appears to be almost constant over the 45–47 kOe field range which may be indicative of multiple phase transitions or a fact that the region of the T-H phase diagram, shown in Fig. 18, that is
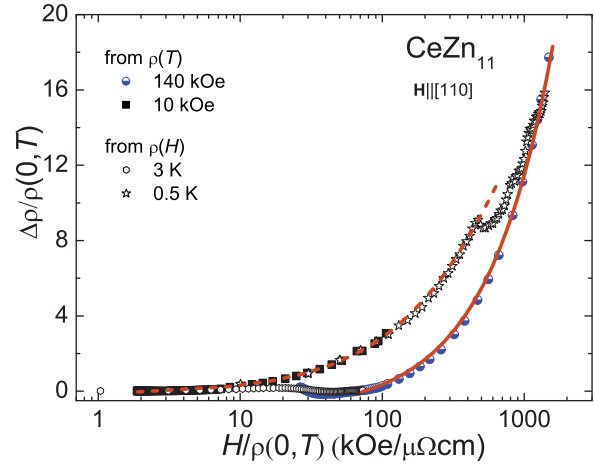

FIG. 11. (Color online) Kohler plot (showing only every third data point), $\Delta\rho/\rho(0,T)$, for the highest and lowest field and temperature, where $\Delta\rho = \rho(H,T) - \rho(0,T)$, for CeZn$_{11}$ for the field applied along the [110] direction. The dashed and solid lines denote two manifolds that the data appear to follow.

centered at this range of magnetic field, is rich and complex. At 1 K, $C_p(H)$ manifests a sharp peak at 40 kOe, which corresponds to a transition from an ordered to a nonordered state, followed by a small, higher-field shoulder that might be related to the first-order nature of the AFM transition. As the magnetic field is further increased, from 47 kOe $< H <$ 90 kOe, C/T gradually drops towards zero, consistent with establishing a low-temperature, saturated paramagnetic state. At 3 K, only a broad feature is observed at ~70.5 kOe in $C_p(H)$. It should be noted that the field-sweep data (solid symbols) agree well with the data taken from temperature sweep in constant magnetic field (open symbols) that were shown in Fig. 12. To shed further light on the field-induced states of CeZn$_{11}$ for $\mathbf{H} \parallel$ [110], we measured the Hall resistivity ρ_H and thermoelectric power S.
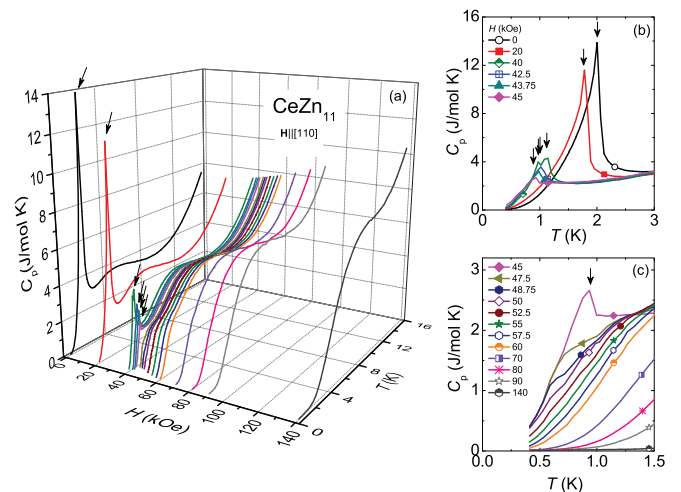

FIG. 12. (Color online) (a) Heat-capacity data for CeZn$_{11}$ taken with the applied magnetic field $\mathbf{H} \parallel$ [110], (b) and (c) expanded, low-temperature part of heat-capacity curves. The arrows indicate peaks associated with the magnetic ordering.
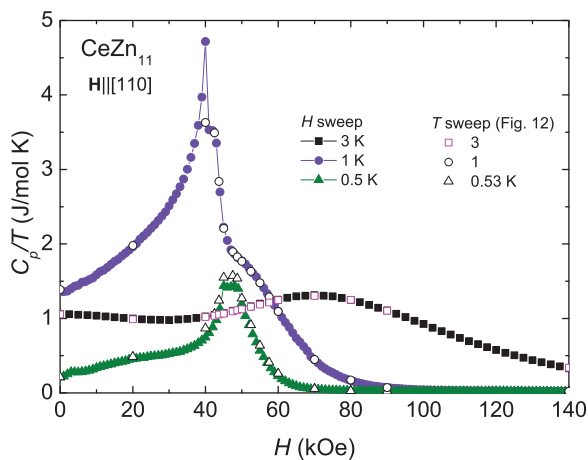
FIG. 13. (Color online) C_p/T of CeZn$_{11}$ as a function of magnetic field measured at constant temperatures of 0.5, 1, and 3 K (solid symbol data) with the magnetic field along the [110] direction. Open symbols represent the data taken from $C_p(T)|_{H=\mathrm{const}}$ shown in Fig. 12.

Figure 14 shows $\rho_H(H)$ measured at several constant temperatures. For the temperatures higher than 25 K, ρ_H is positive and almost linear. For temperatures 10 K and below, ρ_H not only becomes nonlinear, but also changes sign from positive to negative. As the temperature is decreased, the field at which ρ_H changes sign moves toward lower applied magnetic fields. As will be discussed in the following, the sharp, low-field feature seen in the lowest-temperature data is associated with the transition from the low-field, AFM state to a higher-field state that is most likely a saturated paramagnetic state. To see this feature more clearly and to track its progression as we increased the temperature, we subtracted the linear background, represented by a dashed line in the main graph. The result is shown in the inset to Fig. 14. The sharp peak, which corresponds to the AFM transition at the two lowest temperatures, evolves into a broad peak positioned at
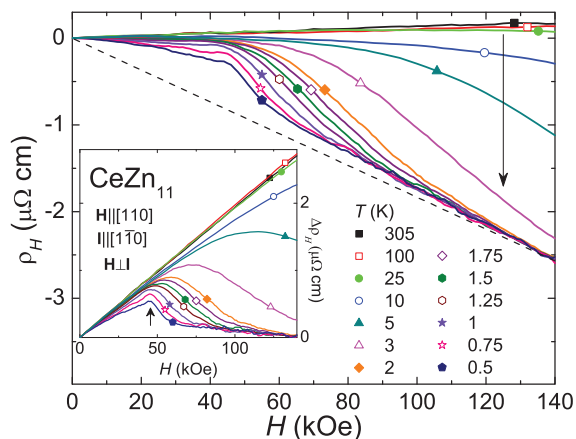

FIG. 14. (Color online) Hall resistivity $\rho_H(H)$ of CeZn$_{11}$ measured at different constant temperatures. The inset shows the data after the linear background, represented by a dashed line on the main graph, is subtracted. The arrow indicates the field of the maximum which corresponds to a transition from an ordered to a nonordered state at the lowest temperature. (The data sets were smoothed with the adjacent-point-averaging method with a 5 points of window.)
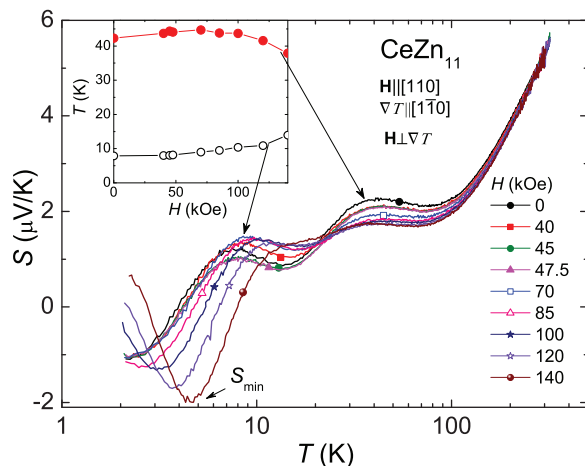

FIG. 15. (Color online) The semilog plot of the temperature-dependent thermoelectric power $S(T)$ of CeZn$_{11}$ measured with different applied magnetic fields $\mathbf{H} \parallel [110]$. The inset illustrates the evolution of the two local maxima as a function of applied field.

a higher applied field as the temperature is increased. CEF effects are probably the origin of this broad feature. The discussion of the Hall coefficient R_H is given in the Appendix.

Figure 15 shows a semilog plot of the temperature-dependent thermoelectric power $S(T)$ of CeZn$_{11}$ taken at different applied magnetic fields. As the applied field is increased, the temperature of the peak positioned at ~40 K first moves slightly up, and then moves more rapidly down and that of the lower peak at ~8 K moves up and starts to merge with the lower-temperature tail of the one at ~40 K at 140 kOe. Above ~100 K, the TEP is essentially unchanged by increasing magnetic field and has an almost linear temperature dependence. For $H = 0$, TEP reverses the sign at 4 K: $S < 0$ for $T < 4$ K. As the applied field is increased, the temperature at which the sign is changed moves to the higher temperatures. For $H \geqslant 120$ kOe, the TEP changes sign twice. For example, for $H = 120$ kOe, $S > 0$ for $T > 6.3$ K and $T < 2.2$ K. Within the experimental temperature window accessible with our current measurements, it is not possible to determine exactly the magnetic field at which the TEP starts to change sign a second time, although it seems that the required field is closer to $H = 120$ kOe rather than to $H = 100$ kOe.

The TEP as a function of the field $S(H)$, taken at 2.3 K, is plotted in Fig. 16 and has a complex behavior. Quantum oscillations are seen above ~70 kOe in the $S(H)$. The amplitude of the quantum oscillations observed in the TEP is much larger than those observed in other measurements, which is a unique aspect of the TEP because, rather than depend on the density of states at the Fermi level, it depends on the derivative of the density of states evaluated at the Fermi level.[34,35] This is often a very useful method of studying quantum oscillations in Ce-based compounds.[35] Fast Fourier transform (FFT) analysis of the quantum oscillations seen in the TEP measurements is given in the inset to Fig. 16 and shows strong peaks in the FFT spectrum at ~2.0 MOe (α), ~4.1 MOe (β), ~5.9 MOe (γ), ~10.2 MOe (δ), ~12.4 MOe (ε), and ~14.4 MOe (ζ). To obtain the FFT spectrum, we took the last 1024 data points and subtracted the background that was fitted with the polynomial function. After that, the data
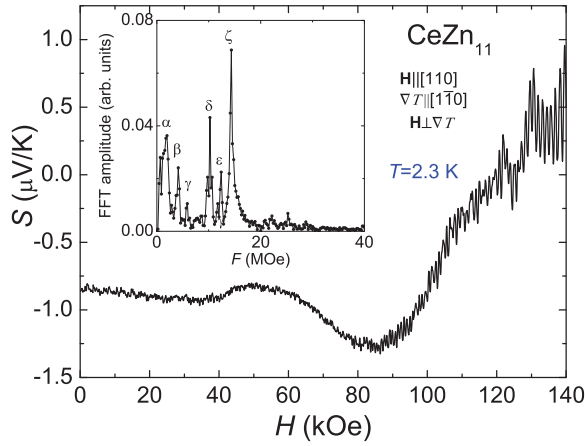
FIG. 16. (Color online) (a) Field-dependent thermoelectric power $S(H)$ of CeZn$_{11}$ at 2.3 K. The inset: FFT spectrum of the oscillations obtained from TEP at 2.3 K.

were plotted in $1/H$ and interpolated so that the 1024 data points were equally spaced. After that, the FFT analysis was done.

IV. DISCUSSION

CeZn$_{11}$ orders antiferromagnetically near 2 K. On one hand, the zero-field temperature-dependent resistivity shows a broad shoulder, characteristic of that of Kondo compounds. On the other hand, the close proximity of the Schottky anomaly to the low AFM transition makes it hard to obtain or estimate the Sommerfeld coefficient γ precisely and as a result to tell to what extent the density of states at the Fermi level is enhanced. According to Ref. 36, at the characteristic temperature T_K, for a system that does not order magnetically, the entropy reached by a Kondo system is $0.65R\ln2$. For CeZn$_{11}$, $0.65R\ln2$ of entropy is reached at ∼2 K meaning that $T_K < T_N$, possibly much less. The Kondo temperature can also be estimated from the paramagnetic Curie-Weiss temperature as $T_K = |\Theta_p|/4$.[37] From our Curie-Weiss law fit of the polycrystalline average (see Table I), $\Theta_p = -5.6 \pm 1.0$ K which translates into $T_K = 1.4 \pm 1.0$ K, which agrees with the T_K obtained from the entropy. These estimates, taken together with our other data, indicate that $T_N > T_K$ and possibly $T_N \gg T_K$. As we discussed above, our estimates of γ associated with CeZn$_{11}$, which were done for $T \gg T_K$, yield a value that is a little bit larger or equal to that of LaZn$_{11}$. This means that at least in $H = 0$, the system is essentially not strongly correlated.

Changing the applied magnetic field along the [110] direction suppresses the AFM transition temperature of CeZn$_{11}$ and allows us to map the T-H phase diagram and possibly find quantum critical point (QCP) effects. The criteria that were used to map the T-H phase diagram were mentioned on several occasions above. The criteria for inferring the AFM transition temperature T_N from the specific heat C_p and derivatives of resistivity $d\rho/dT$ (Ref. 22) and magnetic susceptibility $d(\chi T)/dT$ (Ref. 21) data were shown in Fig. 7(b). In $d\rho/dT$ data in addition to the sharp peak at 1.93 ± 0.07 K, which corresponds to T_N, another broad shoulder is evident at 3.6 ± 0.5 K [denoted by an arrow in Fig. 17(a)]. This broad
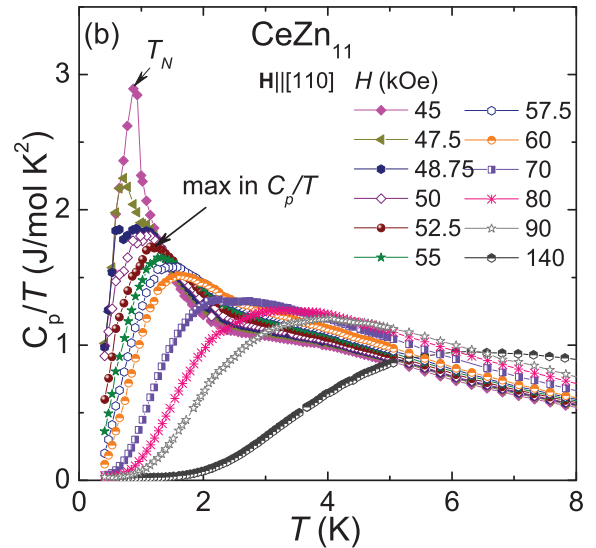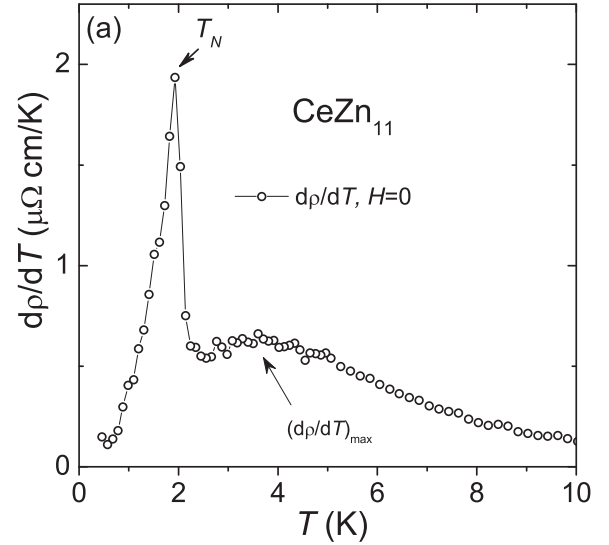

FIG. 17. (Color online) (a) $d\rho/dT$ as a function of temperature. Arrows denote the AFM transition temperature and a broad shoulder in $d\rho/dT$. The $\rho(T)$ data set was smoothed with the adjacent-averaging method with a 2 points of window before derivative was taken. (b) C_p/T as a function of temperature, arrows indicate a peak associated with the magnetic ordering and the maximum in C_p/T that emerges at $H \geqslant 47.5$ kOe.

feature moves to higher temperatures as the applied field is increased.

In the heat-capacity measurements, as the applied magnetic field is increased, the sharp peak corresponding to the AFM transition moves to lower temperatures and broadens (see Fig. 12). For $H \geqslant 47.5$ kOe, in addition to the broad maximum at low temperatures, another broad peak at slightly higher temperature develops and is more clearly seen in the C_p/T versus T plots [Fig. 17(b)]. This peak becomes broader and moves to higher temperatures as the magnetic field is further increased. It has to be noted that a similar feature in the heat capacity was observed for the YbNiSi$_3$ compound[38] and was attributed to splitting by the applied field of the nearly degenerate crystal-electric-field levels that form the zero-field ground state.

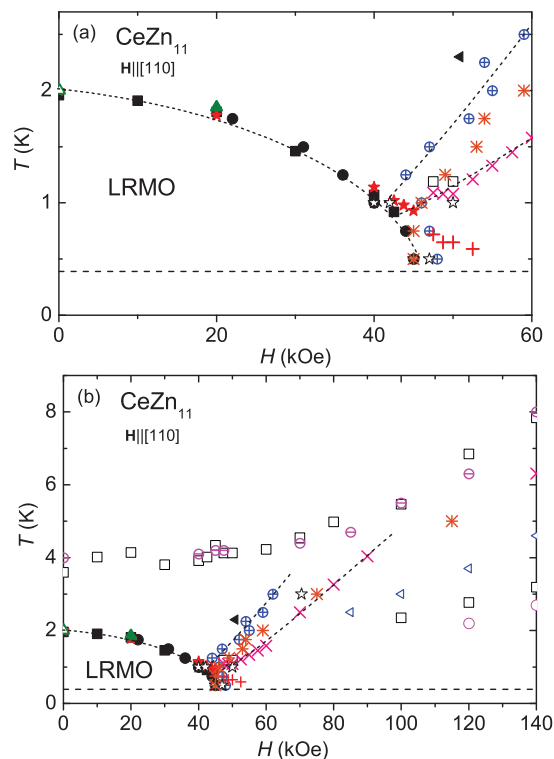FIG. 18. (Color online) (a), (b) H-T phase diagram of CeZn$_{11}$ for **H** ∥ [110]. Long-range magnetic order (LMRO) region is marked on the phase diagram. Legends: ▲: dM/dH; △: d(χT)/dT; ■ and □: dρ/dT (T_N and broad maximum, respectively); ● and ⊕: dρ/dH (T_N and minimum, respectively); ★: C_p (T_N); +: broad peak in C_p; ×: max in C_p/T; open stars: features seen in $C_p(H)$; ∗: maximum in $\Delta\rho_H$; ◁: $S_{\min}$; ⊖: $S_{\pm}$; ○: $S_{\mp}$; and ◀: $S(H)$. Dashed lines that run through the data points are guides to the eye. Dashed line at 0.4 K is the temperature limit of our measurements.

In Fig. 18(a), we present the low-temperature/low-field phase diagram for CeZn$_{11}$, **H** ∥ [110], where, as the applied magnetic field is increased, the AFM order is suppressed below our base temperature of 0.4 K in the 45–47.5 kOe field range and a system is driven to a low-temperature state with no apparent long-range magnetic order. The broad shoulder seen in $C_p(T)$ above 45 kOe [see Fig. 12(c)] is shown as "+" and does seem to follow from the peak in C_p associated with the T_N. Figure 18(a) looks promising in terms of bringing the AFM transition temperature to zero with the modest applied magnetic field.

Figure 18(b) shows the T-H phase diagram over a wider T and H range. The broad Schottky-type features seen in C_p/T (×), the broad minimum observed in dρ/dH (⊕), and the broad maximum in $\Delta\rho_H$ (∗) appear to delineate a broad stripe that starts near the end of the AFM dome and around $H \sim$ 80 kOe starts to move to higher temperature with increasing field along with $S_{\min}$ (◁) and a feature seen in dρ/dT (□). The origin of the slight difference among these features is probably the fact that different measurements see different degrees of scattering off of saturating moments and the CEF levels.

The evolution of the TEP sign change as the system is tuned by the applied magnetic field is also shown in Fig. 18(b) (⊖ and ○). The TEP is negative in-between ⊖ and ○. We would
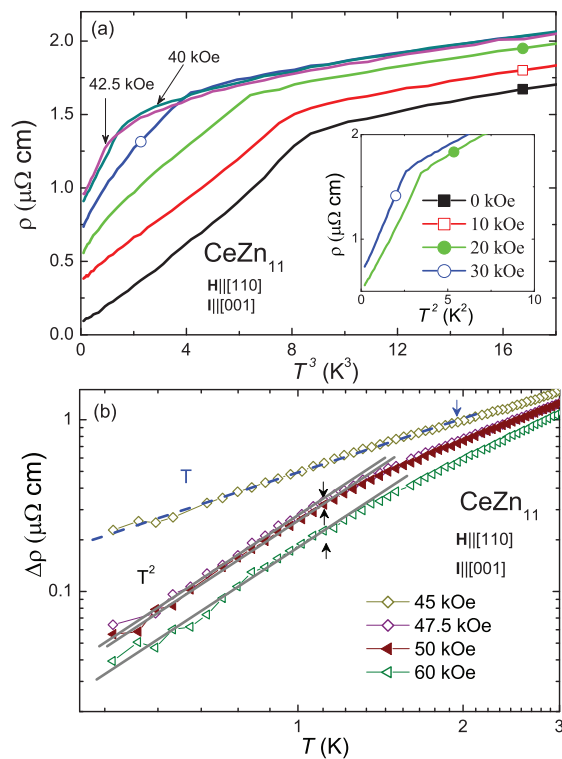

FIG. 19. (Color online) (a) $\rho(T)$ curves for CeZn$_{11}$ taken at different applied fields for **H** ∥ [110] as a function of T^3 (main graph) and T^2 (inset). (b) Log-log plot of $\Delta\rho(T) = \rho - \rho_0$ for CeZn$_{11}$, 45 kOe $\leqslant H \leqslant$ 60 kOe. Dashed and solid lines represent T and T^2 dependencies, respectively. Arrows denote the temperatures where the data deviate from linear and quadratic dependencies.

like to point out that for the TEP setup used, 2.1 K was the lowest temperature reached. Interestingly, the change of the sign of the TEP, $S_{\pm}$ (⊖), coincides with the feature seen in dρ/d$T_{\max}$ (□).

In order to look for the Landau–Fermi-liquid or non–Landau–Fermi-liquid behavior as the AFM transition is suppressed, we further analyzed the resistivity data by performing the fit of the low-temperature part of the resistivity in the form $\rho = \rho_0 + AT^n$, where A is the coefficient and n is the exponent. For the Landau–Fermi-liquid regime, the resistivity is governed by the electron-electron scattering, A is the quasiparticle scattering amplitude, and $n = 2$. When the system is close to the AFM QCP, some theories predict $n \leqslant 5/3$.[2] In the AFM state, the fit results in $n \approx 3$ [Fig. 19(a)], except for the applied fields of 20 and 30 kOe for which $n \sim 2$ [inset to Fig. 19(a)]. Figure 19(b) shows the log-log plot of $\Delta\rho = \rho - \rho_0 = AT^n$ versus T for 45 kOe $\leqslant H \leqslant$ 60 kOe, **H** ∥ [110]. The low-temperature $\rho(T)$ functional dependence for $H = 455$ kOe appears to be linear, $n = 1$, from base temperature of 0.46 to 1.96 K. For the applied fields between 47.5 and 60 kOe, the fit results in $n \sim 2$ marking the region of the Landau–Fermi-liquid behavior. Given that the Landau–Fermi-liquid behavior holds only for a very small temperature range, from ∼1.12 K down to the base temperature of 0.46 K, further resistivity measurements for $T < 0.46$ K will be required to have a larger span of the temperatures for which the Landau–Fermi-liquid regime holds. Ironically, part
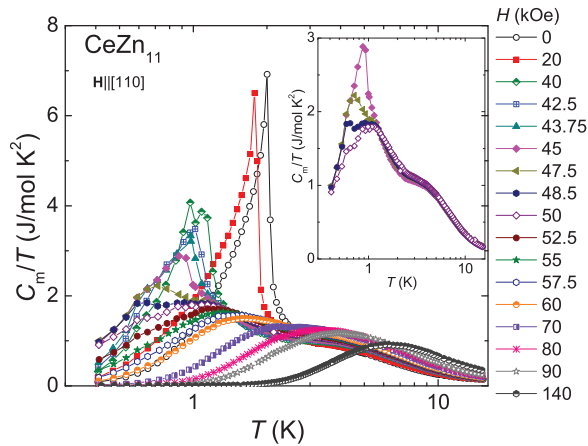
FIG. 20. (Color online) Semilog plot of the magnetic part [$C_m = C_p(\text{CeZn}_{11}) - C_p(\text{LaZn}_{11})$] of the heat capacity C_m/T as a function of T. The inset shows the data sets for 45 kOe $\leqslant H \leqslant$ 50 kOe.

of our difficulty in fitting of low-T, finite-H data may be due to the very high RRR values we can achieve in zero field. As recently shown for PtSn$_4$ (with RRR $\sim$ 1000),[39] simple Kohler's rule magnetoresistance can lead to strong increases in $\rho(T)$ upon cooling in fixed fields. The sum of this normal metal magnetoresistance with the possible Fermi-liquid and non-Fermi-liquid contributions can result in complex, and hard to interpret, temperature dependencies of the resistivity. Indeed, as seen in Fig. 9, the $\rho(T)$ at highest fields appears to be dominated by this large positive magnetoresistance and actually shows a local minimum upon cooling.

To look for non–Landau–Fermi-liquid behavior in the heat-capacity data of CeZn$_{11}$, the magnetic part of the heat capacity C_m/T as a function of temperature is plotted on a semilog plot in Fig. 20. C_m was obtained by subtracting $C_p(\text{LaZn}_{11})$ ($H = 0$) using the assumption that for LaZn$_{11}$ $C_p(T)$ is essentially field independent. Based on the spin fluctuation theories for non-Fermi-liquid behavior of the specific heat proposed by Millis and Hertz, Moriya, and Lonzarich, for an ideal quantum critical system, for $H = H_c$, the heat-capacity data should diverge as $C_m/T|_{T\to 0} \propto -\ln T$ or $C_m/T|_{T\to 0} \propto -\sqrt{T}$ (see Ref. 2 for discussion of the theory) indicating a non–Landau–Fermi-liquid regime. The inset to Fig. 20 shows the data for 45 kOe $\leqslant H \leqslant$ 50 kOe and no such non–Landau–Fermi-liquid-like signature is found.

Figure 20 also clearly shows that for $H \leqslant$ 60 kOe, the electronic specific-heat coefficient γ, which reflects the effective mass of the $4f$ electrons, clearly becomes very small. This is in contrast to such QCP systems such as YbAgGe (Ref. 40) or YbPtBi (Ref. 41), where γ stays significantly enhanced for wide field ranges above H_c. Given our 0.4-K base temperature, we can plot C_p/T at 0.4 K as a function of applied field as shown in Fig. 21(a). As the magnetic field is increased, C_p/T increases, reaches the highest value of 1 J/(mol K) at 47.5 kOe, and then steadily and rapidly decreases to $\sim$18 mJ/(mol K) at $H = 140$ kOe.

Figure 21(b) shows the evolution with field of the resistivity ρ at 0.46 K and ρ_0, obtained from $\ln(\rho - \rho_0) = \ln(AT^n)$ fit. As the applied field is increased, both ρ and ρ_0 show weak features at about $H = 45$ kOe. ρ at 0.46 K increases, reaches
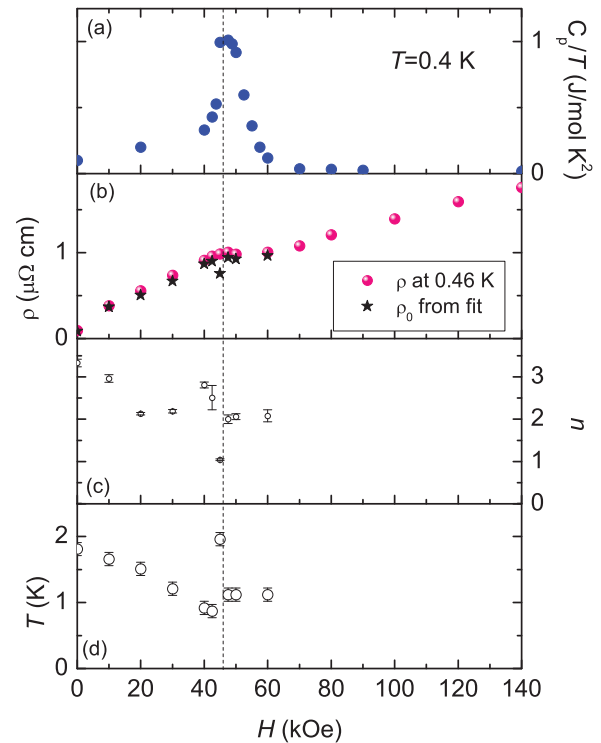

FIG. 21. (Color online) (a) C/T at 0.4 K, (b) resistivity at 0.46 K and ρ_0, obtained from $\ln(\rho - \rho_0) = \ln(AT^n)$ fit, as a function of applied magnetic field. (c) The exponent n from $\ln(\rho - \rho_0) = \ln(AT^n)$. (d) The range of temperatures where $\log(\rho - \rho_0) = \ln(AT^n)$ fit was performed.

a small maximum at 47.5 kOe, then goes through a shallow minimum and increases again. ρ_0 behaves similarly to $\rho|_{0.46\,\text{K}}$ except its value dips only at 45 kOe. Figure 21(c) shows the exponent n from $\ln(\rho - \rho_0) = \ln(AT^n)$ fit. The ranges of temperature that were used to perform the fit are given in Fig. 21(d). The range of temperature was chosen from the base temperature to the point where the data in the log-log plot of $\Delta\rho$ versus T started to deviate from linear behavior. ρ_0 was adjusted so that the resistivity curve at the lowest temperatures appeared linear on the log-log plot. The behavior of residual resistivity and scattered coefficient n near the critical field may indicate that (i) the T_N is almost or just suppressed below 0.46 K in the 42.5 kOe $\leqslant H \leqslant$ 47.5 kOe field range and the temperature region is not sufficiently wide to perform the fit; or (ii) the functional dependence of the resistivity is altered by the remnant AFM transition (which is hard to resolve in our resistivity data), and lower temperature is required to perform the fit; or (iii) taking into account that the T-H phase diagram is quite crowded in the 42.5 kOe $\leqslant H \leqslant$ 47.5 kOe region and there are actually multiple transitions close to each other that are hard to resolve in our resistivity data due to the ΔT step with which the data sets were taken. To resolve these issues, one would need to take the measurements, with tighter data steps, down to lower than our current base temperature. Hence, taken as a whole, Fig. 21 is more consistent with a quantum phase transition, similar to what is shown in Refs. 38 and 42, which does not manifest any critical behavior. It becomes evident that CeZn$_{11}$ manifests a local-moment-like metamagnetic phase transition as a function of field.

V. CONCLUSION

We have studied the electrical, magnetic, and thermal properties of single crystals of CeZn$_{11}$ by the means of magnetization, resistivity, specific heat, Hall coefficient, and thermoelectric power. Based on the analysis of our measurements, CeZn$_{11}$ may be classified as essentially a local-moment system with little or no electronic correlations arising from the Ce 4f subshell, with $T_K < T_N \sim 2$ K, and very likely $T_K \ll T_N$. Rather low CEF energy-level splitting is influencing the transport and thermodynamic properties of the compound. CeZn$_{11}$ manifests a strong anisotropy between the tetragonal c direction and the (ab) plane (mild in-plane anisotropy) with the [110] direction being the easy axis. The Hall coefficient is constant at high temperatures followed by a sign reversal at low temperatures. Thermoelectric power shows an almost linear temperature dependence at high temperatures and reverses the sign below 4 K at zero applied magnetic field. Both Hall resistivity and thermoelectric power are positive at high temperatures indicating hole-type carriers dominating the transport properties of CeZn$_{11}$. The T-H phase diagram indicates that the applied magnetic field drives the AFM order temperature below 0.4 K, our lowest temperature measured, by $H \sim 45$–47.5 kOe for **H** ∥ [110]. For the easy axis, **H** ∥ [110], the linear behavior in the $\rho(T)$ data was observed only for $H = 45$ kOe at 0.46 K $\leqslant T \leqslant$ 1.96 K, followed by the Landau–Fermi-liquid regime for the limited range of the applied magnetic field 47.5 kOe $\leqslant H \leqslant$ 60 kOe. No non–Landau–Fermi-liquid behavior was observed in the heat-capacity data. Most likely, as the AFM transition is suppressed, for the magnetic field applied along the easy [110] axis, we observe a quantum phase transition, maybe even of the first order, as is the case for local-moment rare-earth metamagnetism rather than a field-induced quantum critical point.

APPENDIX

1. Analysis of the dHvA oscillation of LaZn$_{11}$

To measure the dHvA oscillations in LaZn$_{11}$, the applied field was varied in constant intervals of $1/H$ in the 37–70 kOe field range for **H** ∥ [110] and **H** ∥ [001]. To separate quantum oscillations from the observed data, the linear background magnetization was subtracted point by point. The resultant magnetization as a function of inverse field is plotted in Fig. 22. The fast Fourier transforms (FFTs) of these data are shown in Fig. 23. The frequencies of the dHvA oscillations for **H** ∥ [110] are smaller than the ones observed for **H** ∥ [001]. For **H** ∥ [110], three large-amplitude peaks are present at 0.23 MOe (α),
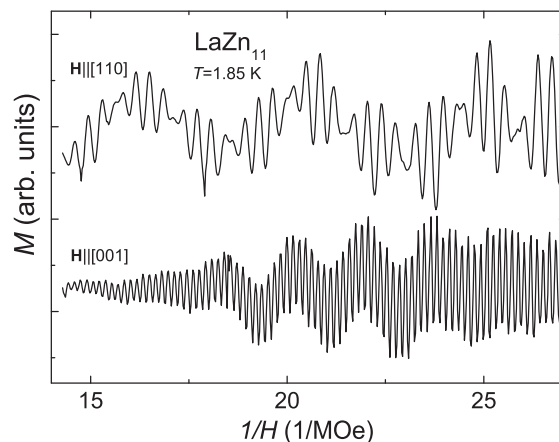
FIG. 22. Magnetization isotherms of LaZn$_{11}$ for **H** ∥ [110] and **H** ∥ [001] at $T = 1.85$ K plotted versus $1/H$.

2.51 MOe (γ), and 3.21 MOe (δ). A smaller-amplitude peak is present at 0.47 MOe (β). For **H** ∥ [001], a large-amplitude peak is present at 6.32 MOe (δ_1) and smaller-amplitude peaks can be found at 0.32 MOe (α_1), 0.55 MOe (β_1), 4.34 MOe (γ_1), and 12.63 MOe (ε_1). The frequencies of β and β_1 are almost the same. The frequencies for LaZn$_{11}$ obtained from the FFT are much smaller then those obtained for CeZn$_{11}$ (see inset to Fig. 16).

The effective masses calculated from the temperature dependence of the FFT amplitudes A of the oscillations can be used to determine the effective masses of the orbits with the help of the Lifshitz-Kosevitch equation[43]

$$M = -2.602 \times 10^{-6} \left(\frac{2\pi}{HA''} \right)^{1/2}$$
$$\times \frac{GFT \exp(-\alpha px/H)}{p^{3/2} \sinh(-\alpha pT/H)} \sin \left[\left(\frac{2\pi pF}{H} \right) - \frac{1}{2} \pm \frac{\pi}{4} \right],$$

where $\alpha = 1.47(m/m_0) \times 10^5$ Oe/K, A'' is the second derivative of the cross-sectional area of the Fermi surface with respect to the wave vector along the direction of the applied field, G is the reduction factor arising from the electron spin, F is the
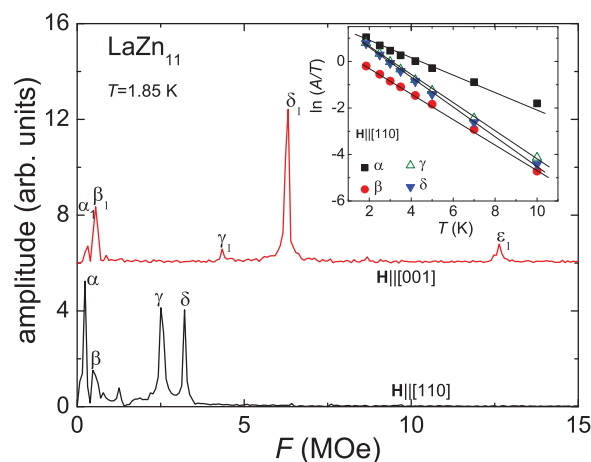

FIG. 23. (Color online) FFT spectra of the dHvA data of LaZn$_{11}$ for **H** ∥ [110] and **H** ∥ [001]. Inset: temperature dependence of the FFT amplitudes A of the observed oscillations for **H** ∥ [110].
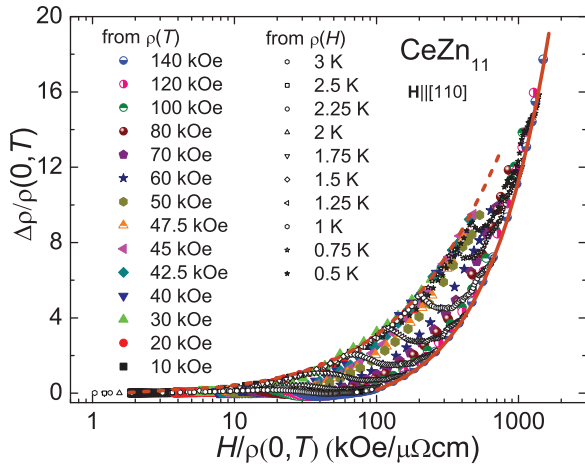
FIG. 24. (Color online) Kohler plot (showing every third data points), $\Delta\rho/\rho(0,T)$, where $\Delta\rho = \rho(H,T) - \rho(0,T)$, for CeZn$_{11}$ for the field applied along the [110] direction. The dashed and solid lines denote two manifolds that the data appear to follow.
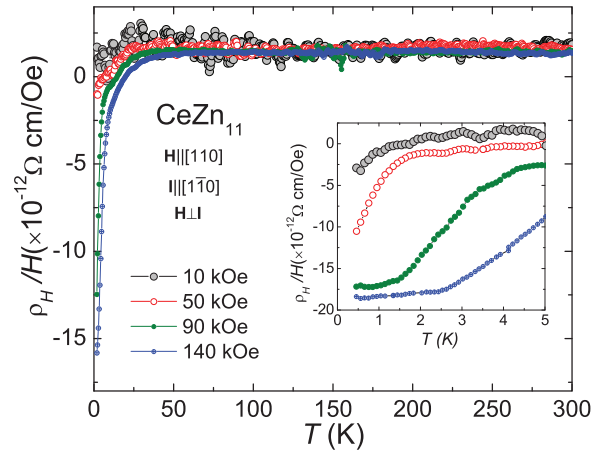

FIG. 25. (Color online) Hall coefficient $R_H = \rho_H/H$ versus temperature for CeZn$_{11}$ at $H = 10, 50, 90,$ and 140 kOe. The inset: low-temperature part of the Hall coefficient data. (The data sets were smoothed with the adjacent-point-averaging method with a 5 points of window.)

frequency of an orbit, p is the number of the harmonic of the oscillation, and x is the Dingle temperature.

From the slope of $\ln(A/T)$ plotted as a function of temperature, the inset to Fig. 23, the effective masses for LaZn$_{11}$ for $\mathbf{H} \parallel [110]$ were found to be $m_\alpha = 0.11(1)m_0, m_\beta = 0.18(1)m_0, m_\gamma = 0.20(1)m_0,$ and $m_\delta = 0.11(1)m_0$, where m_0 is the bare electron mass.

2. Kohler plot

Figure 24 shows the Kohler plot for all the fields and temperatures measured. For clarity, only every third data points are shown. The dashed and solid lines represent the two manifolds that the data appear to follow in the AFM ($[H/\rho(0,T)]^{0.7}$) and paramagnetic ($[H/\rho(0,T)]^1$) states.

3. Hall coefficient

Figure 25 shows the Hall coefficient $R_H = \rho_H/H$ for CeZn$_{11}$. Above 50 K, R_H is essentially temperature and field

independent with the positive value indicating that holelike carriers dominate in the electrical transport, which is consistent with what was observed in the zero-field TEP data in Fig. 8. Upon cooling below 1.8 K for $H = 10$ kOe, R_H changes sign from positive to negative. The temperature at which R_H changes sign increases with the increase of the applied field. At $H = 140$ kOe, R_H changes sign at ~20 K. The features seen at low temperatures (see inset to Fig. 25) in the data for $H = 50, 90,$ and 140 kOe possibly are related to a crossover from $\omega\tau \gg 1$ to $\omega\tau \ll 1$ limit (ω is the cyclotron frequency) which are correlated with the dHvA oscillations that were seen in the resistivity data in Fig. 10.[32] In the one-band approximation, the carrier density at 300 K is $n \simeq 4.46 \times 10^{28}$ m^{-3} ($R_H = 1.4 \times 10^{-12}$ Ω cm/Oe) and is closer to the carrier density of silver $\simeq 5.86 \times 10^{28}$ m^{-3} rather than to that of zinc $\simeq 13.2 \times 10^{28}$ m^{-3}.[44] Although it might be useful for some context, we would like to remark that the one-band and $m = m_e$ approximation is a gross oversimplification when applied in the CeZn$_{11}$ case.

*Currently at the Lawrence Berkeley National Laboratory (LBL).

†Currently at the National Institute of Standards and Technology (NIST).

[1]G. R. Stewart, Rev. Mod. Phys. **56**, 755 (1984).

[2]G. R. Stewart, Rev. Mod. Phys. **73**, 797 (2001).

[3]G. R. Stewart, Rev. Mod. Phys. **78**, 743 (2006).

[4]O. Stockert and F. Steglich, Annu. Rev. Condens. Matter Phys. **2**, 79 (2011).

[5]Y. Nakazawa, M. Ishikawa, S. Noguchi, and K. Okuda, J. Phys. Soc. Jpn. **62**, 3003 (1993).

[6]Z. Fisk, G. R. Stewart, J. O. Willis, H. R. Ott, and F. Hulliger, Phys. Rev. B **30**, 6360 (1984).

[7]H. R. Ott, H. Rudigier, P. Delsing, and Z. Fisk, Phys. Rev. Lett. **52**, 1551 (1984).

[8]S. Yoshiuchi, T. Takeuchi, M. Ohya, K. Katayama, M. Matsushita, N. Yoshitani, N. Nishimura, H. Ota, N. Tateiwa, E. Yamamoto, Y. Haga, H. Yamagami, F. Honda, R. Settai, and Y. Ōnuki, J. Phys. Soc. Jpn. **79**, 044601 (2010); J. Tang and K. A. Gshneidenr, Jr., J. Magn. Magn. Mater. **75**, 355 (1988).

[9]O. Zelinska, M. Conrad, and B. Harbrecht, Z. Kristallogr. New Cryst. Struct. **219**, 357 (2004).

[10]P. C. Canfield, in *Solution Growth of Intermetallic Single Crystals: A Beginners Guide, Properties and Applications of Complex Intermetallics*, edited by E. Belin-Ferre' (World Scientific, Singapore, 2010), p. 93.

[11]P. C. Canfield and Z. Fisk, Philos. Mag. B **65**, 1117 (1992).

[12]S. Jia, N. Ni, S. L. Bud'ko, and P. C. Canfield, Phys. Rev. B **80**, 104403 (2009).

[13] *Binary Alloy Phase Diagrams*, 2nd ed., edited by T. Massalski and H. Okamoto (ASM, Materials Park, OH, 1990).

[14] A. Berche, M.-C. Record, and J. Rogez, Open Thermodynam. J. **3**, 7 (2009).

[15] A. Berche, P. Benigni, J. Rogez, and M.-C. Record, CALPHAD: Comput. Coupling Phase Diagrams Thermochem. **36**, 65 (2012).

[16] H. Okamoto, J. Phase Equilib. Diffus. **32**, 76 (2011).

[17] ftp://ftp.ansto.gov.au/pub/physics/neutron/rietveld/Rietica_LHPM95.

[18] http://www.qdusa.com/sitedocs/appNotes/mpms/1014-201.pdf.

[19] E. Mun, S. L. Bud'ko, M. S. Torikachvili, and P. C. Canfield, Meas. Sci. Technol. **21**, 055104 (2010).

[20] A. Iandelli and A. Palenzona, J. Less-Common Met. **12**, 333 (1967).

[21] M. E. Fisher, Philos. Mag. **7**, 1731 (1962).

[22] M. E. Fisher and J. S. Langer, Phys. Rev. Lett. **20**, 665 (1968).

[23] M. Bouvier, P. Lethuillier, and D. Schmitt, Phys. Rev. B **43**, 13137 (1991).

[24] E. Gopal, *Specific Heat at Low Temperatures* (Plenum, New York, 1966).

[25] A. Tari, *The Specific Heat of Matter at Low Temperatures* (Imperial College Press, London, 2003).

[26] F. J. Blatt, P. A. Schroeder, C. L. Foiles, and D. Greig, *Thermoelectric Power of Metals* (Plenum, New York, 1976).

[27] D. Jaccard, A. Basset, J. Sierro, and J. Pierre, J. Low Temp. Phys. **80**, 285 (1990).

[28] W. Franz, A. Grießel, F. Steglich, and D. Wohlleben, Z. Phys. B **31**, 7 (1978).

[29] D. Jaccard and J. Sierro, in *Valence Instabilities*, edited by P. Wachter and H. Boppart (North-Holland, Amsterdam, 1982), pp. 409–413.

[30] V. Rowe and P. Schroeder, J. Phys. Chem. Solids **31**, 1 (1970).

[31] R. J. Elliott, *Magnetic Properties of Rare Earth Materials* (Plenum Press, London, 1972).

[32] A. Abrikosov, *Fundamentals of the Theory of Metals* (Elsevier, Amsterdam, 1988).

[33] A. B. Pippard, *Magnetoresistance in Metals* (Cambridge University Press, Cambridge, UK, 1989).

[34] R. Fletcher, J. Phys. F: Met. Phys. **11**, 1093 (1981).

[35] E. D. Mun, S. L. Bud'ko, and P. C. Canfield, J. Phys.: Condens. Matter **23**, 476001 (2011).

[36] H.-U. Desgranges and K. Schotte, Phys. Lett. A **91**, 240 (1982).

[37] G. Gruner and A. Zawadowski, Rep. Prog. Phys. **37**, 1497 (1974).

[38] S. L. Bud'ko, P. C. Canfield, M. A. Avila, and T. Takabatake, Phys. Rev. B **75**, 094433 (2007).

[39] E. Mun, H. Ko, G. J. Miller, G. D. Samolyuk, S. L. Bud'ko, and P. C. Canfield, Phys. Rev. B **85**, 035135 (2012).

[40] S. L. Bud'ko, E. Morosan, and P. C. Canfield, Phys. Rev. B **69**, 014415 (2004).

[41] E. D. Mun, S. L. Bud'ko, C. Martin, H. Kim, M. A. Tanatar, J.-H. Park, T. Murphy, G. M. Schmiedeshoff, N. Dilley, R. Prozorov, and P. C. Canfield, Phys. Rev. B **87**, 075120 (2013).

[42] L. S. Wu, Y. Janssen, C. Marques, M. C. Bennett, M. S. Kim, K. Park, S. Chi, J. W. Lynn, G. Lorusso, G. Biasiol, and M. C. Aronson, Phys. Rev. B **84**, 134409 (2011).

[43] D. Shoenberg, *Magnetic Oscillations in Metals* (Cambridge University Press, Cambridge, UK, 1984).

[44] N. W. Ashcroft and N. D. Mermin, *Solid State Physics* (Brooks/Cole Cengage Learning, Belmont, 1976).